Fluid Dynamics & Materials Processing
DOI:10.32604/fdmp.2020.012237
Article

Tech Science Press

Effects of Heaving Motion on the Aerodynamic Performance of a Double-Element Wing in Ground Effect

Ioannis Oxyzoglou* **and Zheng-Tong Xie**

Faculty of Engineering and Physical Sciences, University of Southampton, Southampton, SO17 1BJ, UK
*Corresponding Author: Ioannis Oxyzoglou. Email: io1u18@southamptonalumni.ac.uk
Received: 21 June 2020; Accepted: 18 November 2020

Abstract: The broad implication of the paper is to elucidate the significance of the dynamic heaving motion in the aerodynamic performance of multi-element wings, currently considered as a promising aspect for the improvement of the aerodynamic correlation between CFD, wind tunnel and track testing in race car applications. The relationship between the varying aerodynamic forces, the vortex shedding, and the unsteady pressure field of a heaving double-element wing is investigated for a range of mean ride heights, frequencies, and amplitudes, using a two-dimensional (2D) unsteady Reynolds-averaged Navier-Stokes (URANS) approach and an overset mesh method for modelling the moving wing. The analysis of the results shows that at high frequencies, i.e., $k \geq 5.94$ and amplitudes $a/c \geq 0.05$ the interaction of the shear vorticity between the two elements results in the generation of cohering leading and trailing edge vortices on the flap, associated to the rapid variation of thrust and downforce enhancement. Both the occurrence and intensity of these vortices are dependent upon the frequency, amplitude, and mean ride height of the heaving wing. The addition of the flap significantly alters the frequency of the shed vortices in the wake and maintains the generation of downforce for longer time in ground proximity. The comparison with the static wing provides evidence that the dynamic motion of a race car wing can be beneficial in terms of performance, or detrimental in terms of aerodynamic correlation.

Keywords: CFD; URANS; aerodynamics; heaving wing; multi-element wing; vortex shedding; ground effect; downforce; overset mesh; race car

1 Introduction

Most of the studies on heaving motion of wings are focused on the optimum propulsive performance inspired by flapping flight of insects or birds and they mostly refer to low Reynolds numbers [1], hence the flow physics differ significantly from racing car applications. There are few studies found in the literature regarding heaving wings in ground effect. Moryossef et al. [2] were the first who numerically investigated the flow field of an oscillating airfoil in proximity to the ground. Thereafter, similar studies have been conducted based on numerical simulations and experimental measurements mostly at high Reynolds number with turbulent flows [3]. However, these studies were limited to single-element heaving wings where mostly the frequency-dependent features such as the incidence effect, added mass effect and

ground effect were investigated at various frequencies. Badoe et al. [4] found that the influence of Reynolds number to the lift coefficient of a heaving airfoil is minimal, while the effect on the drag coefficient can be more evident. The sinusoidal motion of a heaving wing can improve its aerodynamic performance in the force reduction region at certain frequencies and is capable of postponing the stall at lower ride heights [5]. Furthermore, at low frequencies, the flow is quasi-stationary and is mostly controlled by the ground effect, while effective incidence effects [6] prevail at medium frequencies. Since lift is a function of the angle attack, the lift will be maximum with the wing at the mean ride height and minimum at maximum (h_{max}) and minimum (h_{min}) ride heights respectively. Additionally, at high frequencies, the added mass effect is dominant [6], regardless of the mean ride height. However, in most race care applications, the heaving motion usually occurs at low frequencies for instance when the nose dives during braking and the front wing pitches down, or at high frequencies due to the presence of friction effects on tyres or the highly turbulent incoming flow [7].

During the oscillation of a heaving wing, there are three primary vortex shedding patterns that may occur, based on which the wake is classified into drag, thrust, or neutral producing wake. The value of the critical reduced frequency for thrust generation depends on the heaving amplitude and ground proximity of the wing [8]. In the case of a drag-producing wake, the upper row of vortices consists of clockwise rotating vortices, while in the case of a thrust-producing wake the top row of vortices has an anticlockwise rotation [9]. To this extent, Wang et al. [10] stated that the rotational orientation of the vortex mushroom itself is indicative of thrust or drag producing wake, since when the mushroom cap is tilted towards the streamwise direction the wake generates thrust, whereas the wake induces drag when the mushroom cap is pointing to the upstream direction. Regarding the application to race cars, it is of great interest to study the case of heaving multi-element wings in ground effect. Therefore, the focus of the present study is on the investigation of the instantaneous force distribution of a heaving double-element front wing in ground effect, which might provide a more insightful understanding than previous approaches with single airfoils. First, the effect of frequency on the aerodynamics of the heaving wing in freestream and ground effect is addressed, setting the basis for the amplitude sensitivity analysis of the wing under heaving motion.

2 Methodology

2.1 Wing Geometry

The wing geometry used comprised of two 2D elements in a single flap configuration (Fig. 1). The detailed airfoil coordinates were taken from Zerihan [11] with the flap set at the low angle position. The main element chord length was 139 mm and the flap chord length 103.1 mm, with a total wing chord length (c) of 238.17 mm, based on which all the length scales were normalized. Due to the lack of literature data for heaving double-element wings, the validation of the model was done using only the main element as a single heaving airfoil, hence all length scales were normalized by 139 mm in these cases. After an experimental optimization with regard to downforce [12], it was found that the optimum overlap (δ_0) and gap (δ_g) were $0.024c$ and $0.032c$ respectively. The origin of the coordinate system is located on the leading edge of the main element with the ride height (h) defined as the vertical distance between the lowest point of the suction surface of the main element and the ground, and the main element and flap incidences (a_m, a_f) set at 3.6° and 15.5° respectively, resulting in a total reference incidence (a_t) of 11.5° for the whole wing. The incidence of the single airfoil was set at 5°.

2.2 Computational Grid

The grid used in this study was a high-quality hexahedral mesh, generated using Trimmed Mesher. The computational domain (Fig. 2) extended $4c$ upstream, $12c$ downstream and $4c$ above the wing, while the distance to the ground varied based on the ride height studied at each case. For the freestream case,

the bottom boundary was 4c from the wing. The outlet of the domain was set in a distance which ensured that at least 10–15 cycles of oscillation were captured in the wake even at the lowest frequency. To simulate the heaving motion, the overset mesh method [13] was employed. This method uses interpolation points connected through interfaces in the overlap region to couple the solutions between different grids [14], thus eliminating the need for remeshing between timesteps. The computational domain was discretized in two separate overlapping regions; with a rectangular block inside the background domain containing only the wing. This block extended 0.25c upstream, 1.5c downstream, 0.5c above and 0.05c below the wing to prevent any collision with the prism layers of the ground at the lowest ride height. The overset grid moved together with the oscillating wing as the relative grid topology remained immutable, whereas the overlapping regions shared the same size to prevent any interpolation errors. A non-conformal interface was created between the overlapping regions to couple the overset with the background region, allowing a solution with a low level of iteration errors and a rate of convergence similar to that of a uniform mesh.

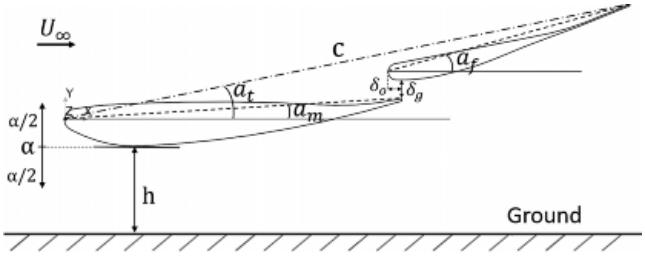

Figure 1: Sketch of the wing geometry and definition of its characteristic parameters

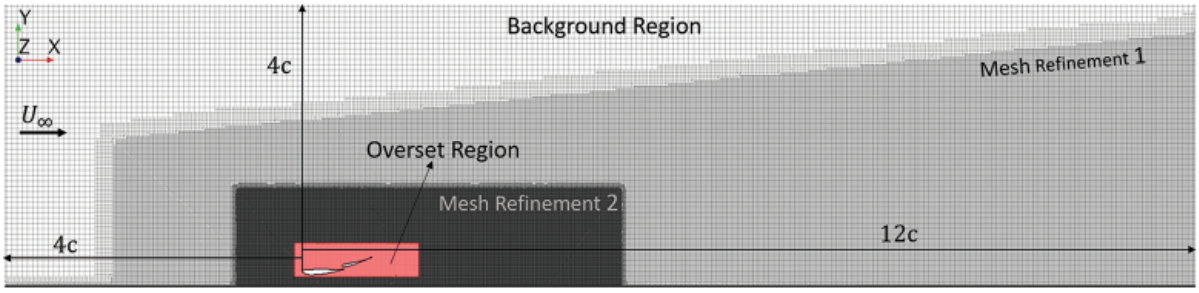

Figure 2: Computational domain used both for static and heaving cases

A total number of 510 and 360 grid points were used across the main element and flap respectively, and 26 prism layers with a growth ratio of 1.2 and a total thickness of 10 mm that were generated inside the boundary layer (Fig. 3a). Special attention was given to the gap between the leading edge of the flap and the trailing edge of the main element, by placing at least 6 cells into the gap that ensured continuity in the cell size as the wing oscillates (Fig. 3b). Similarly, 20 prism layers with an aspect ratio of 1.2 were generated on the ground plane, with a total thickness of 2.5 mm. These mesh settings resulted in a first cell height of 0.035 mm, sufficient to achieve a wall $y^+ \leq 1$, both on the wing and ground surfaces with a "worst" cell skewness angle of 60.4° for the quadrilateral mesh. After a mesh independence study, 521,210 cells were used on the background and 162,768 cells on the overset domain, resulting in a total number of 683,978 cells. The accuracy of the mesh was tested by a direct comparison of the force coefficients with [5,12] under both stationary and heaving wing conditions.

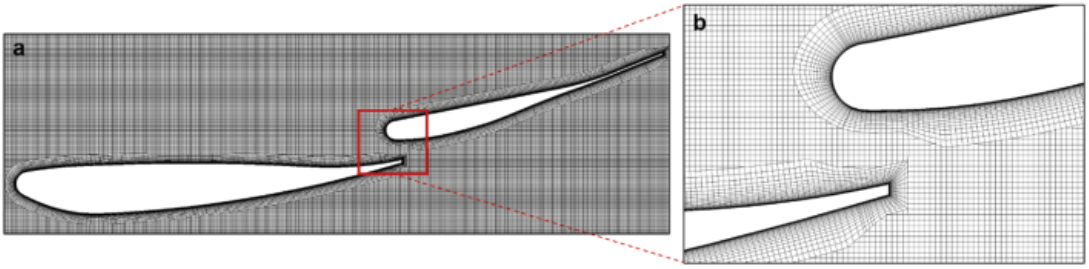

Figure 3: (a) Mesh within the overset region (b) near-wall grid in the gap between the two elements

2.3 Heaving Motion

The dynamic heaving motion of the wing was implemented by means of vertically translating the overset region, using sinusoidal user-defined functions with amplitude α and frequency (f). At the start of each period, the wing was located at the mean ride height (h_0) and it oscillated with an amplitude of $\alpha/c = 0.08$ based on the chord length of the main element for the single airfoil case and the total chord length for the double-element wing case, respectively. The expression for the ride height at each time step is given by:

$$h(t) = h_0 - \frac{\alpha}{2}\sin(2\pi ft) \tag{1}$$

The heaving motion of the overset region that involved the wing as a rigid body was defined using the expression for vertical velocity (v), given by the derivative of the vertical displacement in Eq. (1) as:

$$v = \frac{dh}{dt} = -\alpha\pi f\cos(2\pi ft) \tag{2}$$

The heaving frequency can be nondimensionalized with respect to a characteristic length scale and velocity as:

$$k = \frac{\pi fc}{U_\infty} \tag{3}$$

Eq. (3) represents the reduced frequency, which is the ratio between the time a particle takes to traverse the chord of the wing c/U_∞ in one period of oscillation $1/f$ [5], thus it shows the interference effect between the bound and shed vortices [3]. Additionally, the non-dimensional ride height $(\hat{h})$ and non-dimensional time (τ) of the heaving motion are given respectively:

$$\hat{h} = \frac{h - h_0}{\alpha/2} = -\sin(2\pi ft) \tag{4}$$

$$\tau = \frac{t}{T} = ft \tag{5}$$

All the following results in the frequency and amplitude sensitivity analyses of the heaving motion will be presented as a function of the dimensionless parameters k, $\hat{h}$ and τ.

2.4 Numerical Method

The flow field was computed using a 2D pressure-based incompressible CFD solver for the unsteady Reynolds Averaged Navier-Stokes (URANS) within STAR-CCM+. The averaged continuity equation is:

$$\frac{\partial U_i}{\partial x_i} = 0 \tag{6}$$

and the averaged momentum equations are:

$$\frac{\partial \rho U_i}{\partial t} + \frac{\partial (\rho U_i U_j)}{\partial x_j} = -\frac{\partial P}{\partial x_i} + \frac{\partial}{\partial x_j}\left[\mu \frac{\partial U_i}{\partial x_j}\right] - \frac{\partial \overline{\rho u_i' u_j'}}{\partial x_j} \tag{7}$$

where U_i is the averaged velocity, P is the averaged pressure, ρ is the fluid density, μ is the dynamic viscosity, u_i' is the fluctuating velocity and $\overline{\rho u_i' u_j'}$ is the Reynolds stress [13]. The latter was modelled based on the eddy viscosity concept, hence assumed to be proportional to the averaged velocity gradients and turbulent viscosity [15]. The accuracy of URANS for oscillating airfoils is substantially related to the competence of the turbulence model [16], hence the one equation Spalart-Allmaras model was employed as it captures better the unsteady separated flow at low subsonic Mach numbers over the standard two-equation models [15]. The URANS equations were solved using the finite volume method, with a 2^{nd}-order upwind discretization for convection terms, a 2^{nd}-order central difference scheme for diffusion terms, and a 2^{nd}-order implicit scheme with 30 internal iterations per time step for the time integration. The SIMPLE pressure-velocity coupling scheme was employed to enforce mass conservation and obtain the velocity and pressure fields that satisfied the continuity and Navier-Stokes equations [17].

The upstream boundary was modelled as a velocity inlet with $U = 41$ m/s in the x direction, while the downstream boundary was modelled using the pressure outlet boundary condition, with a gauge pressure of 0 Pa. The symmetry plane condition was imposed at the top boundary of the computational domain to model a zero-shear slip wall, while the wing and ground surfaces were modelled as solid walls with a no-slip condition enforced. Finally, a translational velocity of 41 m/s in the streamwise direction was set to the bottom boundary to simulate the moving ground. The single airfoil simulations for the validation of the heaving case were performed at $\mathrm{Re} = 3.9 \times 10^5$ based on the reference chord length of 139 mm and the freestream velocity. Similarly, all simulations for the frequency and amplitude sensitivity analyses were conducted at a $\mathrm{Re} = 6.68 \times 10^5$ based on the total chord length of 238.17 mm of the double-element wing. In all cases, the wall boundary layer was resolved up to the viscous sub-layer. The turbulence specification within the flow was initialized using a turbulence intensity of 0.3% and turbulent viscosity ratio of 68 at the inlet boundary. The high turbulence levels of the freestream flow at the inlet ensured that the flow was turbulent across the entire wing surface [3], hence reproducing realistic race conditions [5].

Based on a time refinement study conducted in Molina et al. [18], the optimal time step depends on the frequency, hence for transient simulations the nondimensional time step varied from 10^{-3} ($k \leq 0.37$) to 10^{-4} ($k \geq 4.57$). As the frequency decreased, the time step reduced respectively to ensure that unsteady phenomena are captured properly [3], while maintaining an acceptable Courant number ($CFL \leq 1$) in all cells. Moreover, the time step selected ensured that the overset mesh did not move within the overlapping zone more than half the smallest cell size in this zone within a time step [13]. Additionally, at low frequencies where a quasi-stationary solution was obtained, the total simulation time (T_S) was set to capture at least 20 particles traversing the chord section of the wing based on the freestream velocity ($T_S = 20c/U_\infty$). For the initialization of the unsteady simulations, at least five complete cycles of heaving motion were performed until the flow field was stabilized and a quasi-periodic solution was obtained during the oscillation.

3 Model Validation

3.1 Variation of Lift Coefficient with Frequency

Due to the lack of data in the literature on multi-element heaving wings in ground effect, the validation of the heaving motion was conducted in correlation to the numerical results presented by Molina et al. [5] and Liang et al. [19] for a single heaving airfoil. The comparison was based on the variation of C_L with the non-dimensional ride height $\hat{h}$ within a range of low ($k = 0.11$), medium ($k = 0.68$) and high ($k = 1.09$) frequencies both in freestream and at $h_0/c = 0.25$ (Fig. 4). Our results compared with those of the two reference studies were in a quantitative agreement, and especially at low frequency where the deviation from the results of Molina et al. [5] lied within 0.6%. The deviation from the results of Liang et al. [19] at low frequency was slightly higher, especially in ground effect, the deviation reached up to 11.8% since the hysteresis between the upstroke and downstroke was noticeably overpredicted in our results.

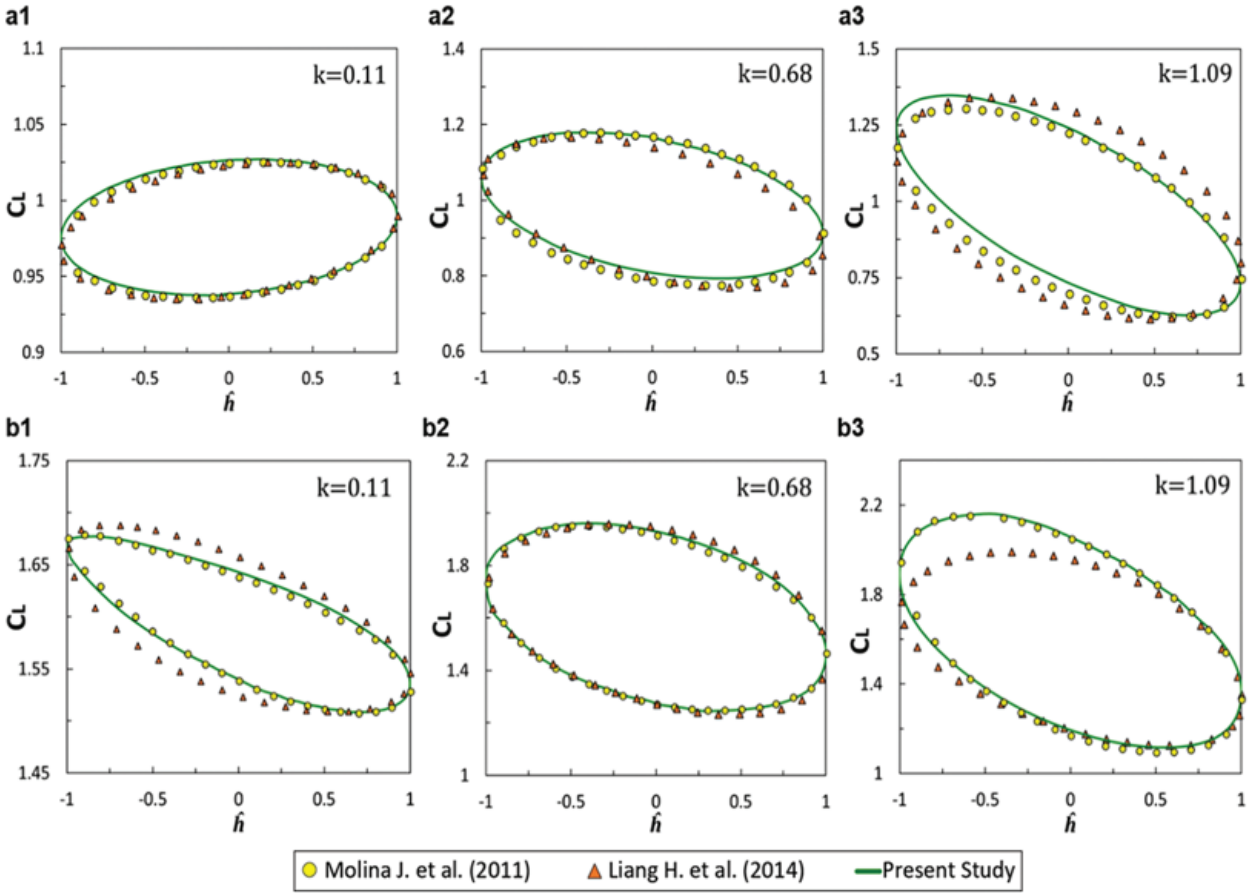

Figure 4: Comparison between the variation of lift coefficient with the non-dimensional ride height (a) in freestream, (b) in ground effect ($h_0/c = 0.25$) for various reduced frequencies

At medium frequency, the present results were more consistent with both the reference studies with a maximum deviation of 2.2% with Molina et al. [5] during the downstroke and a greater difference of 3.6% with Liang et al. [19] during the upstroke in freestream. In ground effect, the difference between the three studies was less than 1.6%. As the frequency increased the variation of C_L was in good agreement with Molina et al. [5] with a maximum deviation of 3.8% in ground effect, whereas in freestream the difference was greater during the downstroke and the deviation at the minimum ride height was around

5.1%. It must be pointed out that the deviation from Liang et al. [19] was also because the effect of viscosity was excluded in their simulations, which was more evident at higher frequencies when the viscosity effect is dominant.

3.2 Vortex Shedding

The qualitative validation of the vortex shedding patterns downstream of the heaving airfoil was focused on the investigation of the effect of reduced frequency and ground clearance on the structure of the wake, compared to the results in Molina et al. [5]. The validation was conducted during the downstroke, with the airfoil at the mean position of $\hat{h} = 0$ and the non-dimensional time $\tau = 1$. Fig. 5 shows the contours of instantaneous non-dimensional vorticity magnitude in the wake at a range of low ($k = 0.55$), medium ($k = 2.18$) and high ($k = 4.37$) frequencies in freestream between the two studies.

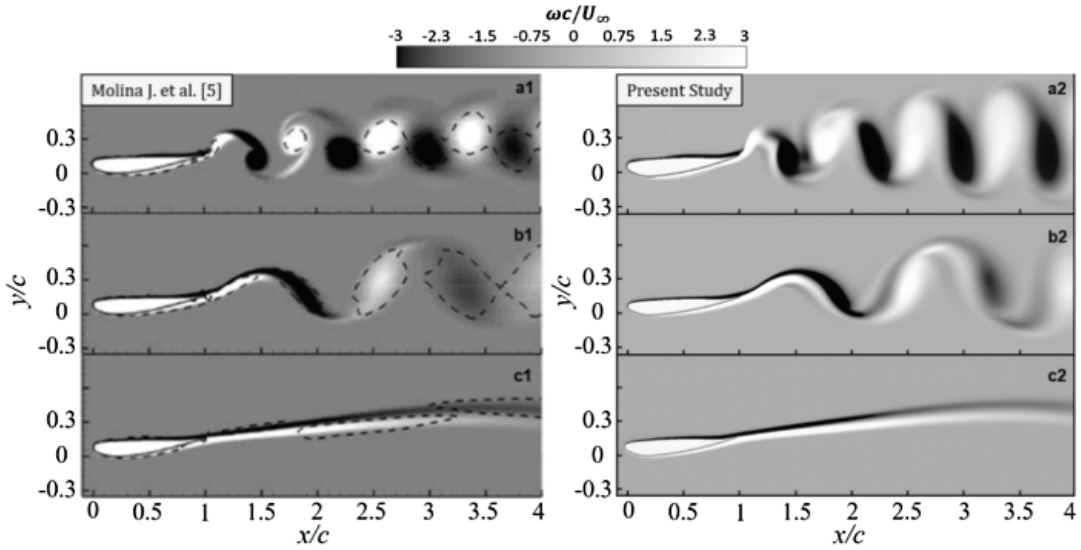

Figure 5: Comparison between the contours of instantaneous non-dimensional vorticity in freestream at $\tau = 1$ and $\hat{h} = 0$ for (a) $k = 4.37$, (b) $k = 2.18$, (c) $k = 0.55$, adapted from [5]

At low frequency (Fig. 5c) the shape of the wake of the present study four-chord lengths downstream of the airfoil matches well with the reference, capturing properly the shear layer and the downward slope of the wake at $x/c = 3.5$. At medium frequency Fig. 5b shows a sinusoidal formation of the vortex patterns in the wake, and the remarkable increase of the wake thickness (t_w), as well as the location of the vortex cores at $x/c = 1.85$ and $x/c = 3.3$ respectively. At higher frequency (Fig. 5a), an alternating vortex shedding pattern was observed with two rows of vortices rotating anticlockwise on the upper row and clockwise on the lower row. The current study was in qualitative agreement with the literature as it accurately captured the location of the cores of the vortices within four chord lengths downstream of the airfoil. Furthermore, the magnitude of these vortices was overpredicted in the present study, and the thickness of the wake at $x/c = 4$ was found to be 13.1% larger, which also confirms the larger deviation found at higher frequencies on the hysteresis analysis.

Next, the heaving motion of the airfoil was validated in ground proximity $h_0/c = 0.25$ and at high frequency $k = 4.37$. Fig. 6 shows that the present study captured the formation of the vortex shedding in the wake, as well as the positive vorticity induced by the trailing edge at $x/c = 1.15$ during the downstroke. The estimation of the locations of the vortex cores at $x/c = 1.45$, $x/c = 2.23$ and $x/c = 2.72$ respectively, was in agreement with the prediction of Molina et al. [5]. However, the distance (a') between the first consecutive clockwise and anticlockwise vortices was found to be 6.9% smaller and

the space (b') between the next two counter-rotating vortices 4.39% bigger respectively, whilst the thickness of the wake at $x/c = 4$ was estimated larger by 11.7%. Additionally, the present study yielded reasonable results on the interaction of the wake with the ground, such as predicting the shear of negative vorticity that built upon the ground at $x/c = 0.5$, the evolution of the two shear layers underneath the vortex cores at $x/c = 2$ and $x/c = 2.72$, and the positive ground vorticity at $x/c = 2.8$. The notable discrepancies in the magnitude of the vortex cores at high frequency, were likely owing to the difference of the moving mesh techniques, the near-wing mesh resolution, and the time integration scheme between the present study and Molina et al. [5]. Overall, the prediction of the cores' streamwise position and the reproduction of the wake patterns for a range of frequencies were promising for the purpose of the validation.

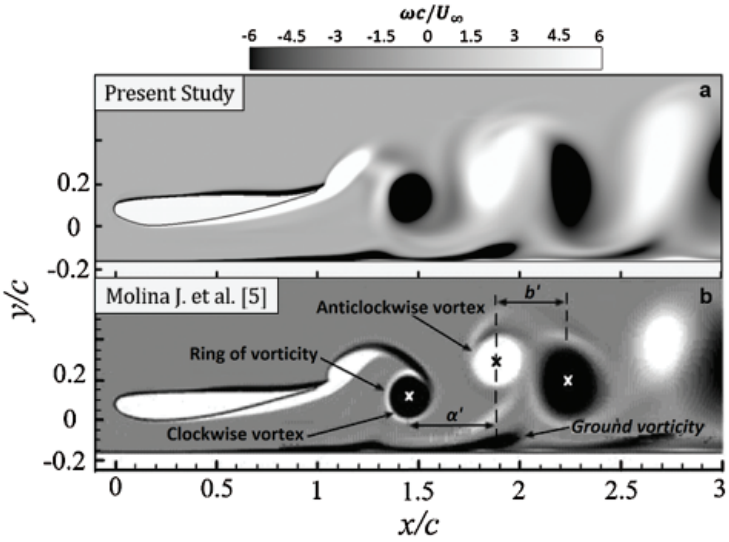

Figure 6: Comparison between the present study and [5] of contours of instantaneous non-dimensional vorticity in ground effect at $h_0/c = 0.25$ for $k = 4.37$, $\tau = 1$ and $\hat{h} = 0$, adapted from [5]

4 Results and Analysis

Depending on the particular behaviour of the stationary wing in a range of ride heights, three main force regions were identified, in accordance with Zhang et al. [12]. The mean ride heights used for the analysis of the heaving motion were selected within these three force regions, and are indicated in red on the C_L curve (Fig. 7). Region 1 was within the Force Enhancement region where the rate of increase of C_L remains low, while Region 2 was also within the Force Enhancement region, but near the C_L plateau and the point of the maximum rate of increase of C_L at $h_0/c = 0.105$. Similarly, Region 3 was between the Enhancement Slow-Down and Force Reduction regions, covering the peak of C_L and the onset of the decrease in the rate of increase of C_L, whereas Region 0 denotes freestream. It is to be noted that the boundaries of each region were defined in reference to an amplitude of $a/c = 0.08$.

The evaluation of the implications of varying frequency and amplitude on the aerodynamic performance of the heaving wing was based on hysteresis plots of C_L and C_D. The clockwise rotation of a hysteresis curve indicates that the wing loses energy to the surrounding air; thus, the motion is more stable, whilst the anticlockwise rotation implies that energy is transferred from the air to the wing, hence inducing instability [5]. Figs. 8 and 9 summarise the hysteresis curves of C_L and C_D respectively for a range of low ($k \leq 0.37$), medium ($0.37 \leq k \leq 1.83$) and high ($k \geq 4.57$) frequencies in freestream, as well as at three different mean ride heights. To accentuate the deviation from the stationary wing, the variation of the static C_L and C_D with ride height is also presented with a dashed line in all plots.

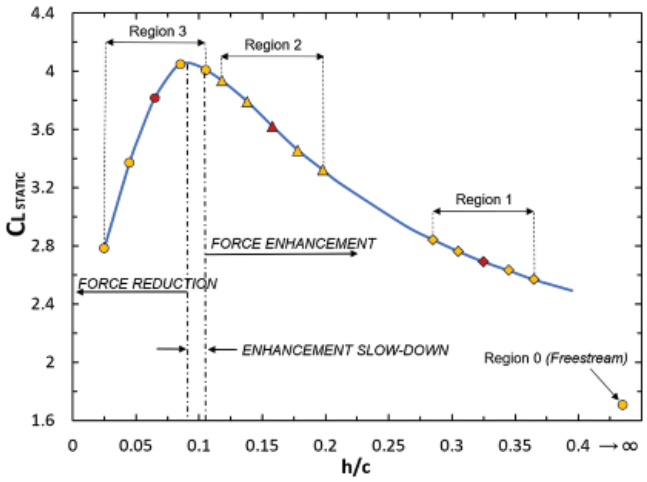

Figure 7: Variation of C_L with ride height for the stationary wing and definition of the heaving regions

4.1 Variation of Lift Coefficient with Reduced Frequency

At low frequencies and out of ground effect (Figs. 8a1 and 8b1) where the incidence effect is dominant, the variation of C_L was symmetrical about the static C_L; hence downforce was greater during the upstroke and maximum at the mean position where the effective incidence is also maximum. At the quasi-stationary state, the hysteresis decreased and tended towards the static C_L where downforce increases with ground proximity due to the ground effect. At lower ride heights (Fig. 8c1) the ground effect was dominant, hence maximum downforce occurred at the lowest position. As the frequency increased (Figs. 8a2 and 8b2) the loops became asymmetrical due to the growing boundary layer separation with the ground proximity (Fig. 8c2). Since the added mass effect was enhanced the hysteresis between the upstroke and downstroke increased respectively, resulting in a higher C_L. On the contrary, at even higher frequencies (Figs. 8a3 and 8b3 and 8c3) the vertical velocity of the wing increased, resulting in larger C_L amplitudes and more instant lift generation. At the Force Reduction region (Fig. 8d3), the static C_L reduced with ground proximity due to the induced flow separation, however, the higher frequencies delayed the wing stall retaining downforce at a high level and the deviation from the static C_L became more evident due to the added mass effect being dominant.

Near the ground and at higher frequencies (Fig. 8d2), the hysteresis grew larger due to the ground effect inducing more downforce during the upstroke than the downstroke; indicative of energy transfer from the wing to the air, and thus a stable state of the wing. However, at the lowest mean ride height and lowest frequencies the direction of the hysteresis curves was reversed (Fig. 8d1), indicative of energy transfer from the air to the wing, thus an unstable state of the wing. The hysteresis curves near the peak of C_L at the lowest position of the wing became smoother and wider, implying that in intense ground effect and low frequencies, downforce was acting on the wing for a longer time, which was in agreement with Molina et al. [5]. At higher frequencies, both in freestream and in ground effect the instant C_L escalated to very large values, almost fourteen times greater than that of the static case (Fig. 8d3). The possible error might be owing to the assumption that the flow was incompressible even at a very high frequency, as well as to the 2D approach that restricted the expansion of the flow only to the streamwise direction.

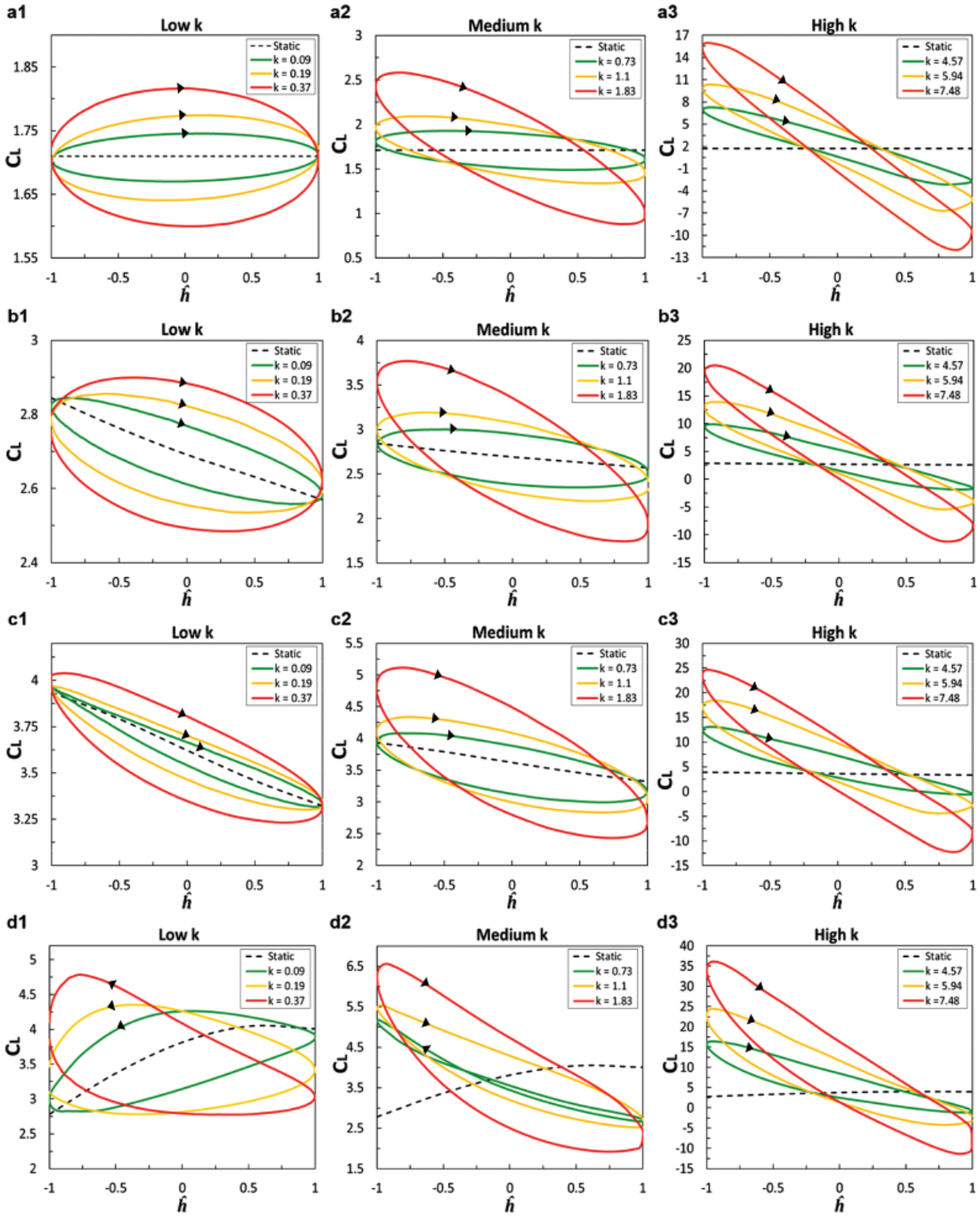

Figure 8: Variation of lift coefficient with non-dimensional ride height for various reduced frequencies (a) in freestream, (b) at $h_0/c = 0.325$, (c) $h_0/c = 0.158$ and (d) $h_0/c = 0.065$

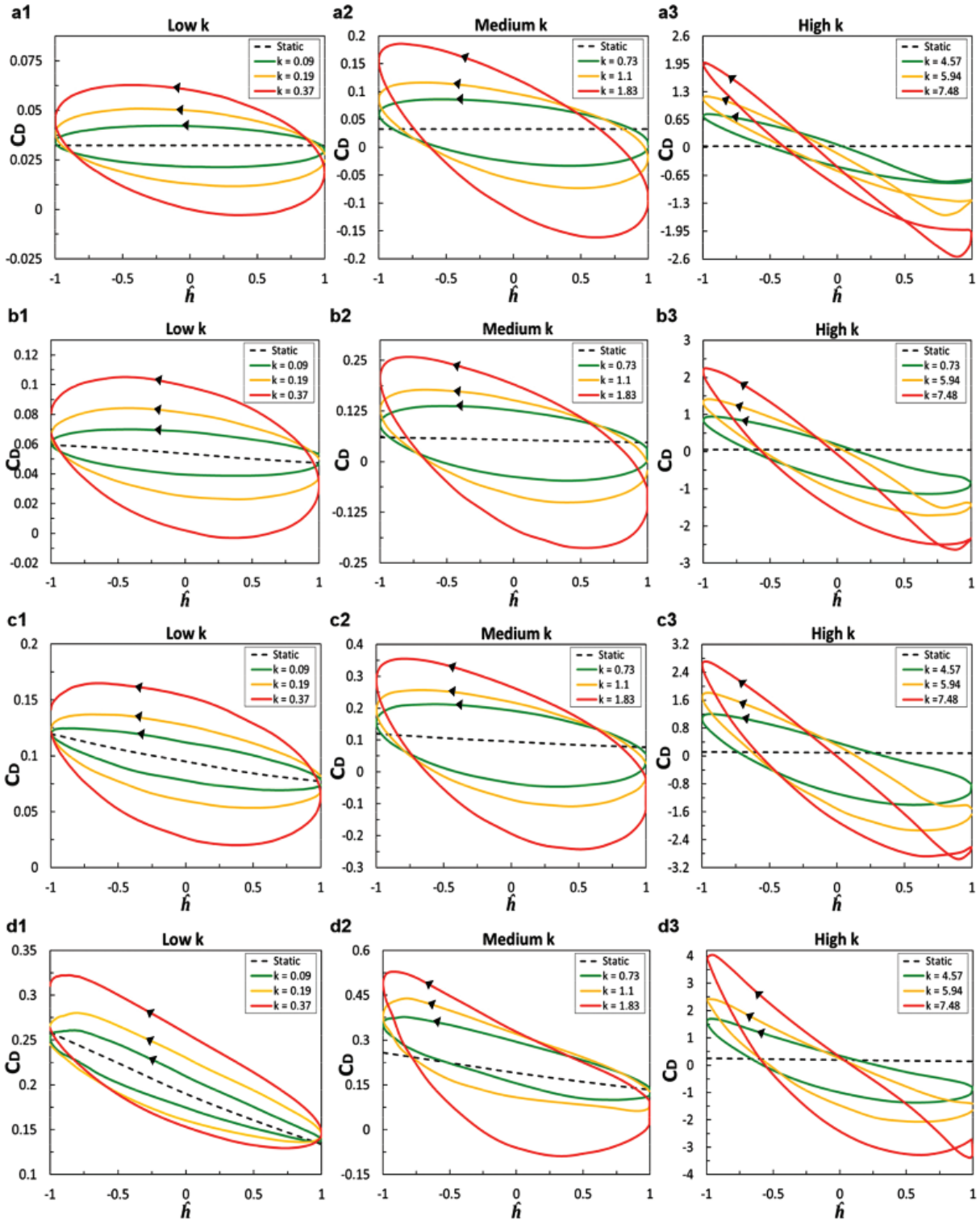

Figure 9: Variation of drag coefficient with non-dimensional ride height for various reduced frequencies (a) in freestream, (b) at $h_0/c = 0.325$, (c) $h_0/c = 0.158$ and (d) $h_0/c = 0.065$

4.2 Variation of Drag Coefficient with Reduced Frequency

Although at $\hat{h} = 0$ downforce was greater during the upstroke in some frequencies, the induced drag was much less or even negative (i.e., thrust), and vice versa during the downstroke. This reversed aerodynamic behaviour was in direct contrast to that of the stationary wing, of which more drag is induced with increased downforce. At low frequencies and out of ground effect (Figs. 9a1 and 9b1) the drag increased with the frequency during the downstroke, while at $k = 0.37$ the induced drag was either zero or negative for a short time during the upstroke. At lower mean ride heights though, drag increased even during the upstroke due to the intense flow separation induced by the ground effect, while at the lowest ride heights there was no evidence of thrust acting on the wing (Figs. 9c1 and 9d1). The variation of C_D at low frequencies remained symmetric about the static C_D even at the lowest ground clearance. At medium frequencies, the hysteresis increased further around the static C_D, and near the ground, the curves became asymmetric due to the increased shear vorticity on the ground. Although the magnitude of the generated thrust near the ground was much greater than in freestream, the shape of the hysteresis curves was identical as the ride height decreased, and the direction of rotation remained anticlockwise within the whole range of frequencies and mean ride heights.

An important observation in accordance with Molina et al. [5] is that when the heaving wing produced drag or thrust at a given frequency in freestream; the equivalent generated amount in ground proximity was noticeably enhanced. At low frequencies, the presence of the ground induced more drag due to the intense flow separation, whereas at medium (Figs. 9c2 and 9d2) and high (Figs. 9c3 and 9d3) frequencies, where the viscous effects are of less importance the hysteresis curves became wider during the upstroke, indicative of maintaining the thrust generation for longer in ground proximity. At all frequencies, the amplitude of the hysteresis curves increased with ground proximity, while the hysteresis between the upstroke and downstroke escalated as frequency increased. For $k \geq 5.94$ at $\hat{h} = 0.5$ in freestream (Fig. 9a3), a point of intersection between the upstroke and downstroke curves was observed and linked to the generation of a cohering leading edge vortex (LEV) on the flap that induced an instantaneous increase of thrust, followed by an increase in drag until the end of the downstroke. However, in ground proximity, this crossover between the two curves was only observed at $k = 7.48$ and with smaller magnitude, as the LEV became weaker due to the interaction with the ground.

4.3 Average Lift and Drag Coefficients

To interpret the overall behaviour of the heaving wing, the average $\bar{C}_L$ and $\bar{C}_D$ of a complete oscillating cycle were analysed using 2D contour plots based on the modified Akima cubic Hermite interpolation. It must be noted that the inverted ratio was used for the ride height, assuming that in freestream $h_0 \to \infty$, hence the $c/h_0 = 0$ represents the freestream case. Although, for frequencies, $k \geq 4.57$ the hysteresis analysis showed that for half of the heaving cycle there was a large production of lift; over the complete cycle the mean vertical force acting on the wing was directed towards the ground (downforce) and was much higher than the static load at the same ride height. At the lower ground clearances and at high frequencies, the $\bar{C}_L$ was almost three times greater than the stationary wing and three times higher than that of the single heaving airfoil, while at low frequencies it approached the static behaviour. Although the $\bar{C}_L$ of the single heaving airfoil increases with ground proximity at all frequencies [5], the $\bar{C}_L$ of the double-element wing (Fig. 10a) was reduced at lower ride heights $c/h_0 \geq 13.8$ but only for a small range of low frequencies $k \leq 2$ where the viscous effects are dominant. Interestingly at ride heights $c/h_0 \leq 12.5$. the $\bar{C}_L$ peaked at $k = 5.94$ after which it started reducing with increasing frequency, in contrast to the single airfoil where the $\bar{C}_L$ increases constantly with frequency at all ride heights.

Similarly to the single heaving airfoil, the $\bar{C}_D$ (Fig. 10b) was constantly decreasing until a critical reduced frequency (k_c) where drag became zero and thrust was produced. The value of k_c varied from $k_c = 2.15$ in freestream to $k_c = 3.45$ at the lowest ride height and is the governing factor for the selection

of the optimum ground clearance and heaving frequency to enhance the aerodynamic performance of the wing. The modified Akima cubic Hermite interpolation was found to be more suitable than the Kriging interpolation used in Molina et al. [5] as it captured slightly better the trend of the maximum average thrust moving to lower mean ride heights at the right boundary of the plot, which would be more evident at frequencies $k \gg 7.48$ that are not covered in this study. Overall, it can be concluded that the presence of the ground can be advantageous at high frequencies, whereas at low frequencies is detrimental, considering that drag increases significantly and downforce is reduced.

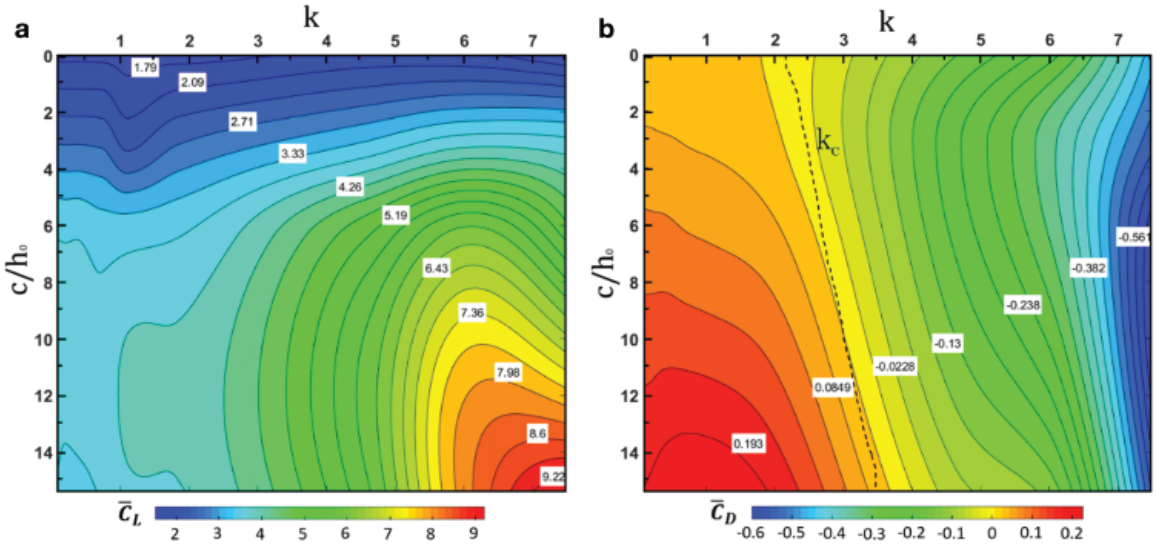

Figure 10: Contours of average (a) downforce and (b) drag generated within a cycle of oscillation, in reference to the mean ride height h_0 and reduced frequency k

4.4 Effect of Frequency on Wake

The investigation of the effects of frequency and ground proximity on the structure of the vortex shedding patterns in the wake was based on the instantaneous non-dimensional vorticity $(\omega c/U_\infty)$. Following figures depict the wing at the mean position of $\hat{h} = 0$ and $\tau = 1$ during the downstroke, at medium $(k = 1.83)$ and high $(k = 7.48)$ frequency. At $k = 1.83$ four shear layers were formed in the wake, with positive vorticity on the suction surfaces and negative vorticity on the pressure surfaces of the flap and main element respectively. The two inner layers of opposite vorticity dissipated earlier due to the higher rate of energy loss, induced by the friction between the inner and outer layers. Both in freestream and weak ground effect, the shear layers adopted a characteristic sinusoidal shape similar to that observed in the single heaving airfoil. At $\hat{h} = 0$ in freestream (Fig. 11a), the shear layer on the pressure side of the flap was almost separated from the surface, while the shear layer on the suction surface of the main element was enhanced by the greater momentum due to the added flap compared to the single wing case. In weak ground effect (Fig. 11b), the shear layer of positive vorticity at the trailing edge of the main element was enhanced by the presence of the ground, where a shear of negative vorticity started to build up.

At lower ride height (Fig. 11c), the shear layer on the suction surface of the main element grew thicker and broke earlier in the wake than in freestream. The distance (λ) between the shed vortices decreased by 11.7% compared to freestream, as the anticlockwise rotating vortex was entrained downstream by the clockwise rotating vortex over the moving ground at $x/c = 3$. The magnitude of the shed vortices was also noticeably enhanced due to the interaction with the shear layer on the ground, while the anticlockwise rotating vortex at $x/c = 3$ lifted the shear layer off the ground. At the lowest ground

clearance (Fig. 11d) the sinusoidal pattern of the wake transformed into a chaotic pattern. The presence of the ground in such small distance, restricted the vertical spread of the shed vortices and enhanced their streamwise expansion, hence the maximum thickness of the wake t_w at $x/c = 3$ decreased by 24.3% compared to freestream. Interestingly, the clockwise rotating vortices at $x/c = 1.5$, $x/c = 1.8$ and $x/c = 3.1$ induced positive vorticity on the ground that was sheared in the opposite direction to that of the moving ground indicating a strong reverse flow locally.

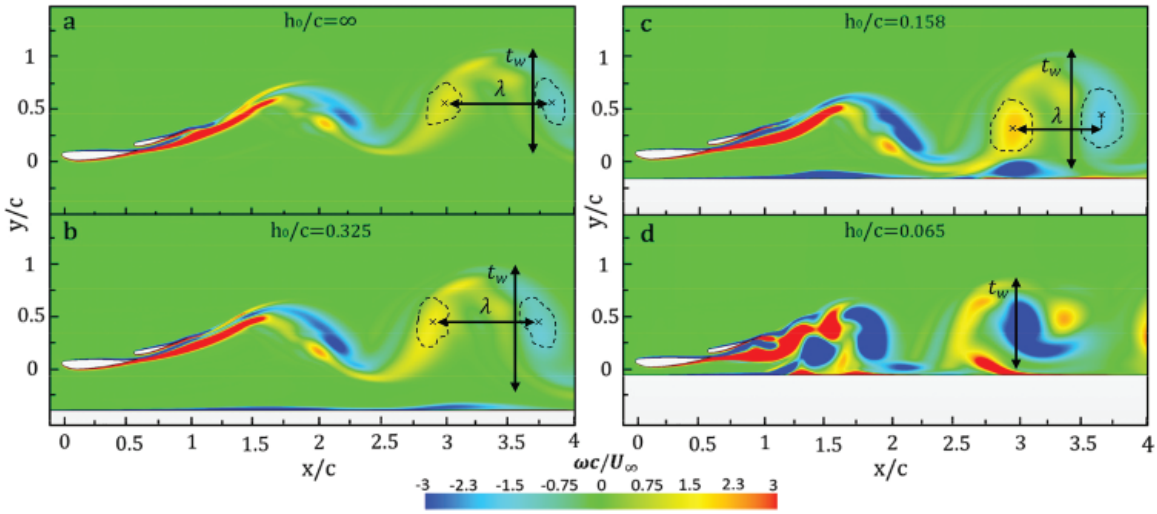

Figure 11: Instantaneous non-dimensional vorticity at $k = 1.83$, $\tau = 1$, $\hat{h} = 0$ at different ride heights

At higher frequency (Fig. 12) the oscillation of the wing became highly energetic inducing an aperiodic jet-like vorticity profile in the wake. Clearly, the crossflow expansion of the wake was substantially greater, as the higher momentum of the heaving wing forced the shear layers to detach earlier to form individual shed vortices. In freestream (Fig. 12a) the vortex shedding patterns formed a thrust producing wake since wake resembled mushrooms of shed vortices were tilted towards the streamwise direction (e.g., at $x/c = 2.25$), indicative of thrust generation [10]. As the ride height decreased further (Figs. 12b and 12c), the arrangement of vortices in the wake consisted of a series of positive vortices rotating above their negative counterparts, adequate evidence of thrust production. As it was shown on the hysteresis analysis of C_D (Fig. 9a3), for frequencies $k \geq 5.94$ a cohering LEV was generated at the leading edge of the flap at the onset of downstroke and was strongly associated to the rapid generation of thrust. With the wing at the mean position during the downstroke, two of these LEV vortices were present on the pressure surface of the flap, until they burst by the upward movement of the trailing edge during the upstroke.

Due to the higher frequency, the shed vortices were formed in proximity to the trailing edge of the flap, and the interaction with the wing became more apparent enhancing the instant production of drag or thrust. The presence of the moving ground in a small distance (Fig. 12c) entrained the shed vortices downstream with higher velocity and deflected the wake downwards at $x/c = 2.75$, compressing it to a thinner film of shed vortices. The thickness of the shear vorticity on the ground was noticeably enlarged by 97.3% compared to that at $h_0/c = 0.325$, while at $x/c = 1.05$ the vorticity layer was lifted off the ground allowing a thin film of positive shear vorticity to grow beneath it. At the lowest mean ride height (Fig. 12d) the complexity of the vortex shedding structure increased dramatically, as the intense interaction with the ground caused a significant upward spread of the wake shortly after $x/c = 1.5$, followed by a severe turbulent breakdown. The maximum amplitude of the wake at $x/c = 3.25$ was surprisingly increased by 72.3% compared to freestream, as the shed vortices were spread up to $1c$ distance above the ground.

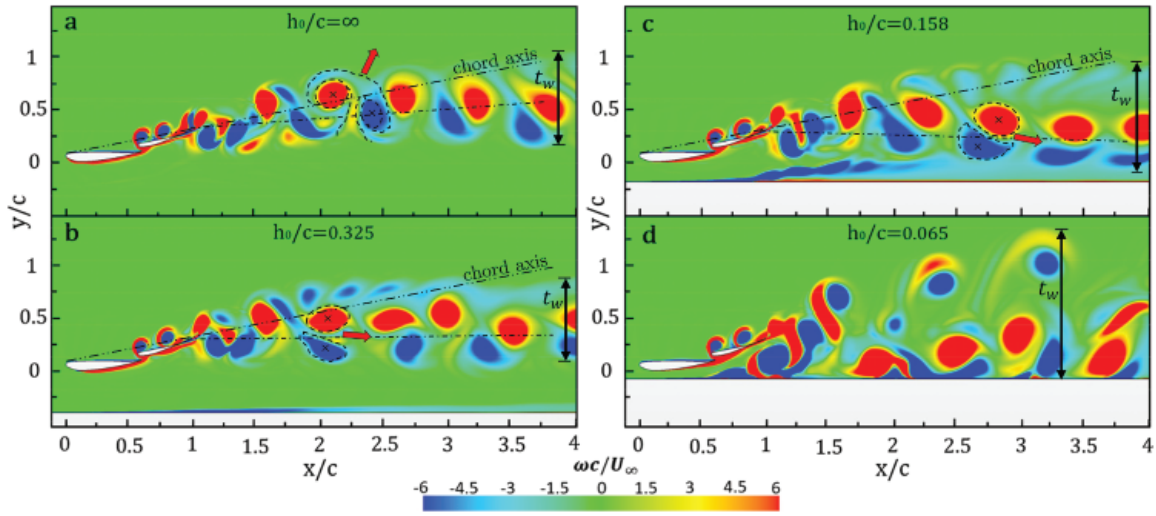

Figure 12: Instantaneous non-dimensional vorticity at $k = 7.48$, $\tau = 1$ and $\hat{h} = 0$ at different ride heights

4.5 Vortex Shedding Evolution

The generation of drag or thrust is strongly depended to the arrangement of the vortex patterns in the wake and the way that the shed vortices interact with the wing. Fig. 13 illustrates step by step the vortex shedding evolution process within a complete heaving cycle for $k = 7.48$ and $h_0/c = 0.158$. The direction of the arrows represents the downstroke ($\downarrow$) and upstroke ($\uparrow$) states respectively. At the onset of downstroke at $\hat{h} = 1$ (Fig. 13g), the downward momentum of the wing forced the positive vorticity from the suction surface of the main element into the narrow gap between the two overlapped elements, causing the negative trailing edge vortex of the main element (TEV_m^-) to detach from the pressure side and move further downstream, before it merges with the combined one of LEV and TEV_f^-. It is believed that this reversed streamwise flow of entrained positive vorticity into the gap was the driving force behind the steep increase of thrust at $\hat{h} = 1$ as shown on the hysteresis analysis. At $\hat{h} = 0.5 \downarrow$ (Fig. 13h), the vertical displacement of the leading edge of the flap enhanced the generation of a cohering clockwise rotating LEV that was eventually rolled up with the positive vorticity filament that was convected from the suction surface of the main element.

At $\hat{h} = 0 \downarrow$ (Fig. 13a) the generated LEV on the pressure surface of the flap was surrounded by a ring of positive vorticity filament. At the trailing edge of the flap, the filament of positive vorticity on the suction side rolled up into a positive trailing edge vortex (TEV_f^+), which later detached at $\hat{h} = -1$. Interestingly, for a quarter of the heaving cycle, two cohering LEVs existed on the pressure surface of the flap since the LEV from the previous downstroke was still present near the trailing edge. With the reverse of moving direction at $\hat{h} = 1$ (Fig. 13c), the positive vortex filament detached from the suction surface of the main element, allowing the LEV to be convected further downstream. One and a half cycles were required for the LEV to traverse across the flap (Fig. 13d) where it eventually burst at $\hat{h} = -0.5 \uparrow$ by the sharp discontinuity of the trailing edge and merged with the weaker TEV_f^- to form a larger clockwise rotating vortex. The upward movement of the wing stretched vertically this clockwise rotating vortex (Fig. 13f) forcing it to detach from the trailing edge of the flap at $\hat{h} = 1$ (Fig. 13g). At $\hat{h} = 0 \downarrow$ (Fig. 13a) the merged vortex of LEV and TEV_f^- of the flap paired up with the incoming TEV_m^- of the main element and eventually, they merged into a greater negative vortex TEV_s^- (Fig. 13f). At $\hat{h} = -1$ (Fig. 13c) the shear layer of negative vorticity on the ground was slightly compressed under the main element. On the contrary, during the upstroke, this shear layer was noticeably lifted off the ground and interacted both with the TEV_f^+ and the TEV_m^- causing the downward deflection of the wake at $x/c = 2.75$.

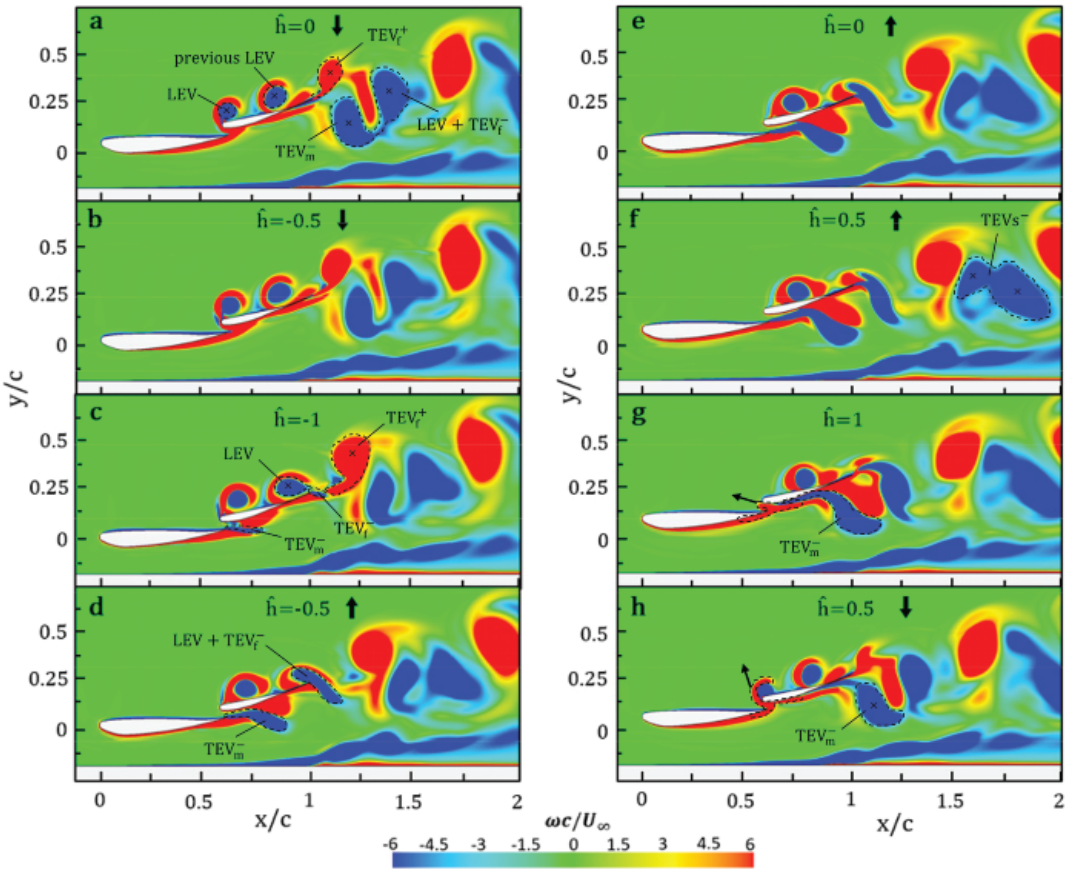

Figure 13: Instantaneous non-dimensional vorticity at $k = 7.48$ and $h_0/c = 0.158$ within a heaving cycle

The substantial amount of reversed flow forced into the gap between the two elements during the downstroke increased the skin friction coefficient (C_f) both on the leading edge of the flap and the trailing edge of the main element. The C_f spikes at the trailing edge of the flap at $\hat{h} = 0$ (Fig. 14a) and $\hat{h} = -1$ (Fig. 14b) were related to the shear of vorticity that led to the generation of the TEV_f^+ and TEV_f^- respectively. At the leading edge of the main element the layer of shear vorticity was much thinner, hence C_f was constantly higher. At $\hat{h} = -1$ (Fig. 14b) the flow was compressed towards the suction surface of the main element, hence C_f was amplified until $x/c = 0.32$. The clockwise vorticity that rolled up at the leading edge of the flap to form the characteristic LEV was manifested through the C_f spike at $x/c = 0.56$. At mid-upstroke (Fig. 14c) the maximum upward momentum of the wing enhanced the acceleration of the flow around the leading edge of the main element, causing a peak of C_f on the pressure surface. Similarly, the upward movement of the wing induced more flow into the gap between the two elements and along the suction surface of the flap resulting in a wider peak of C_f at $x/c = 0.65$. The presence of the entrained LEV on the pressure surface of the flap at $x/c = 2.75$ enhanced the shear of the flow resulting in small fluctuations of C_f. The gradual increase of C_f towards the trailing edge of the flap was caused by the breakdown of the previous LEV due to the upward movement of the trailing edge. At the onset of downstroke (Fig. 14d) the generation of the LEV was triggered by a notable amount of reversed flow near the leading edge of the flap, linked to the C_f spike at $x/c = 2.75$. At $\hat{h} = 1$ the contact between the LEV and the pressure surface of the flap became more intense, hence the substantial peak of C_f at $x/c = 0.77$.

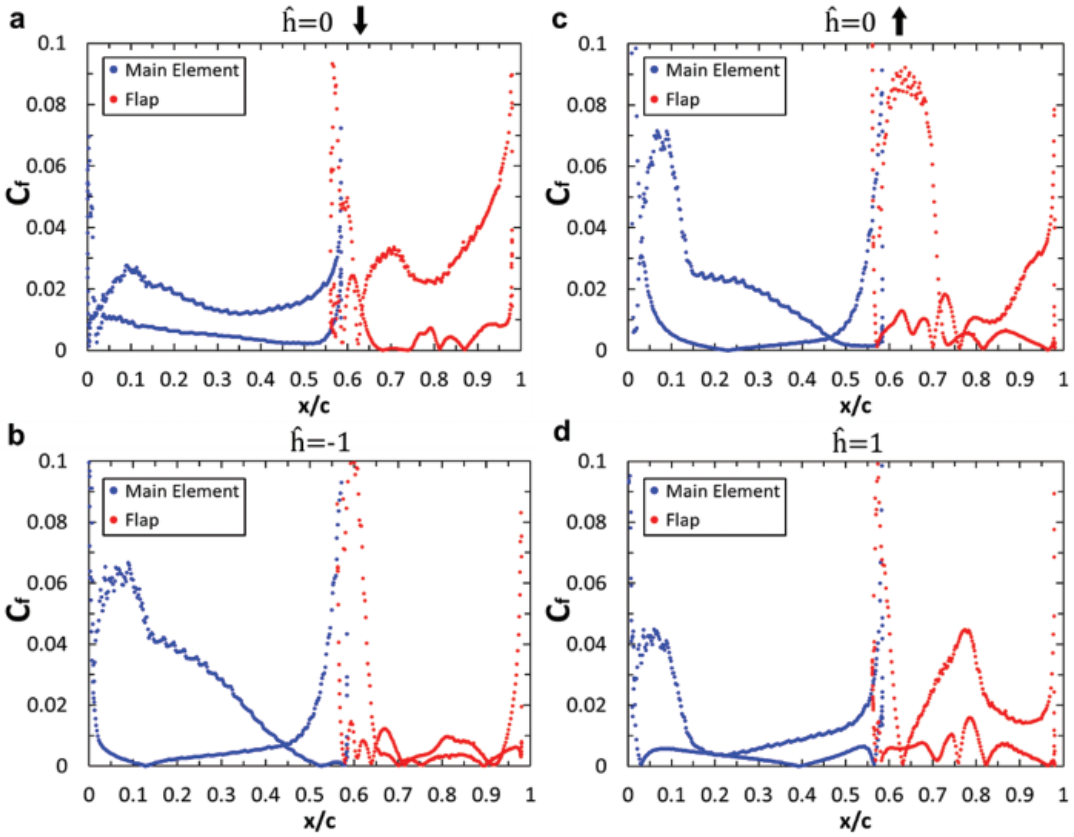

Figure 14: Skin friction coefficient at $k = 7.48$ and $h_0/c = 0.158$ within a cycle of oscillation

4.6 Variation of the Pressure Field

The driving force behind the huge variations in downforce within the heaving cycle was the remarkable change of the pressure field around the wing. Based on Newton's 3rd law, as the heaving wing displaced the air around it, the air applied an equal and opposite reaction on the wing in the form of a pressure force. At $\hat{h} = -1$ (Fig. 15c), the pressure difference (ΔC_P) between the pressure and suction surfaces was maximum, since the wing was displacing the highest amount of air beneath it and the venturi effect enhanced the acceleration of the flow inducing an adverse pressure gradient. Similarly, at the end of upstroke at $\hat{h} = 1$ (Fig. 15g) the wing was displacing air upwards, hence pressure reduced further on the pressure surfaces of the wing inducing lift. However, the ΔC_P at $\hat{h} = 1$ was noticeably smaller due to the weaker ground effect, and this difference in magnitude of downforce and lift resulted in a net average downforce within the complete heaving cycle. As already discussed, the dramatic increase of suction pressure at $\hat{h} = -1$ was connected to the use of an incompressible solver to satisfy the conservation of mass, and the 2D approach that restricted the movement of the air in the third dimension.

During the upstroke at $\hat{h} = 0 \uparrow$ (Fig. 15e), the wing reached its maximum vertical speed, hence the resultant flow velocity (U_{air}) of the vertical velocity $(v_{\max})$ and the streamwise velocity (U_∞) near the maximum curvature of the leading edge of the main flap was higher than any other position. However, at mid-downstroke (Fig. 15a) there was no evidence of such suction peak due to the absence of the ground and the smoother curvature of the leading edge on the pressure surface. In contrast to the single heaving airfoil, the addition of the flap prevented the air from escaping behind the main element at $\hat{h} = -1$, thus a larger amount of air was compressed towards the ground expanding noticeably the low-pressure region in the streamwise direction under the main element. During the upstroke (Fig. 15d), the low-pressure region

was shifted upstream due to the increased flow velocity near the leading edge of the main element, while as the wing decelerated at $\hat{h} = 0.5 \uparrow$ (Fig. 15f) and the ground effect became weaker the suction peak was restricted only on the leading edge. Both the $\text{TEV}_{\text{m}}^{-}$ of the main element and the $\text{TEV}_{\text{f}}^{-}$ of the flap near the suction surfaces of the wing aided to maintain the low pressure under the flap during the upstroke.

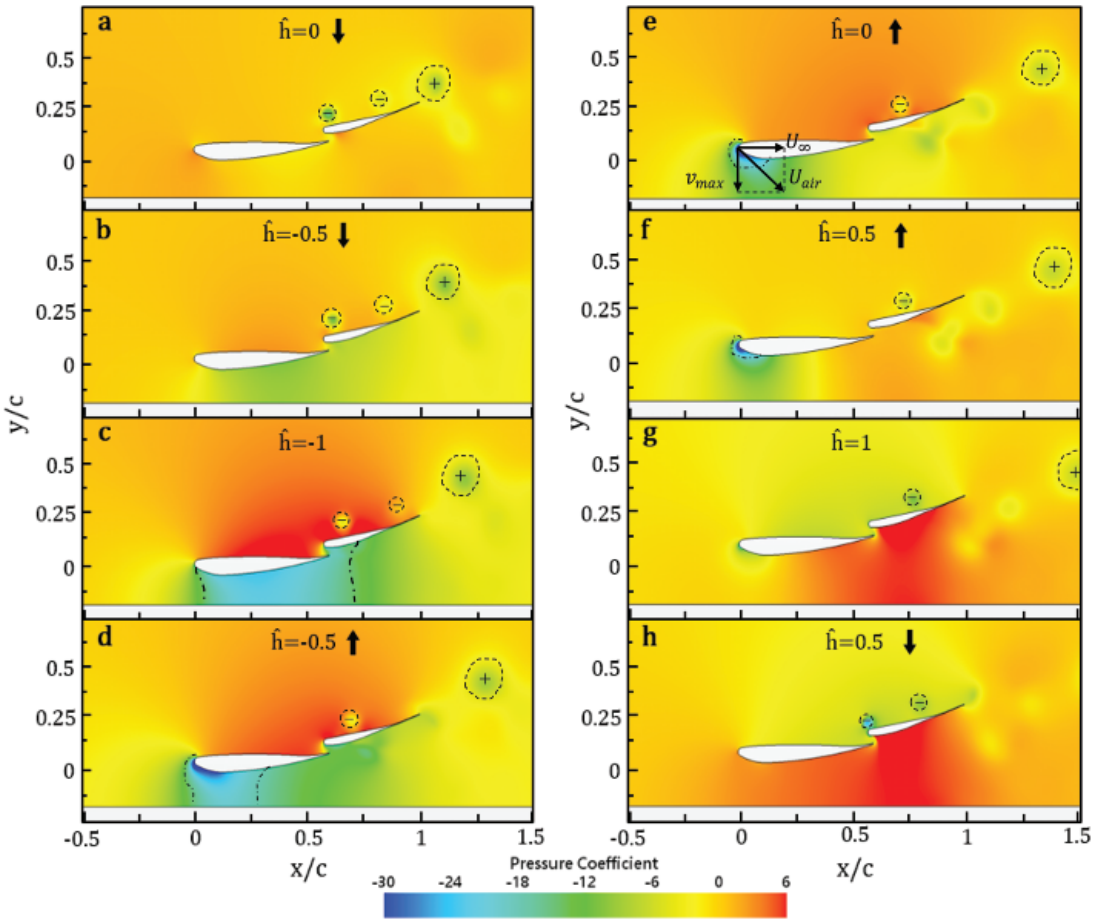

Figure 15: Pressure distribution around the wing at $k = 7.48$ and $h_0/c = 0.158$ within a cycle of oscillation

The heaving motion of the wing induced additional energy into the flow resulting in pressure coefficient (C_P) values greater than unity. The magnitude of the suction peaks varied according to the magnitude and proximity of the shed vortices to the wing. At $\hat{h} = 0 \downarrow$ (Fig. 16a) the suction pressure on the main element decreased, but near the leading edge the pressure was still recovering, while the suction peak on the pressure surface occurred due to the maximum local acceleration of the flow there. On the flap, the pressure was higher on the suction surface with a notable peak at $x/c = 0.63$ induced by the incoming positive vorticity from the suction surface of the main element. The noticeable suction spike at the trailing edge was induced by the low pressure in the $\text{TEV}_{\text{f}}^{+}$ core, while the suction peaks at $x/c = 0.6$ and $x/c = 0.83$ on the pressure surface were linked to the newly generated LEV and the LEV from the previous downstroke respectively. At $\hat{h} = -1$ (Fig. 16b) the pressure recovery occurred near the trailing edge of the flap. On the pressure surfaces pressure was approximately 14 times greater than at $\hat{h} = 0 \downarrow$, resulting in the maximum pressure difference ($\Delta C_{P_{\text{max}}}$) within the whole heaving cycle. However, the interaction with the low pressure within the LEVs at $x/c = 0.65$ and $x/c = 0.9$ was still apparent, indicative of the

great magnitude of these vortices. The steep pressure drop at the trailing edge of the main element and flap was linked to the generation of the $\text{TEV}_{\text{m}}^{-}$ and $\text{TEV}_{\text{f}}^{-}$ respectively.

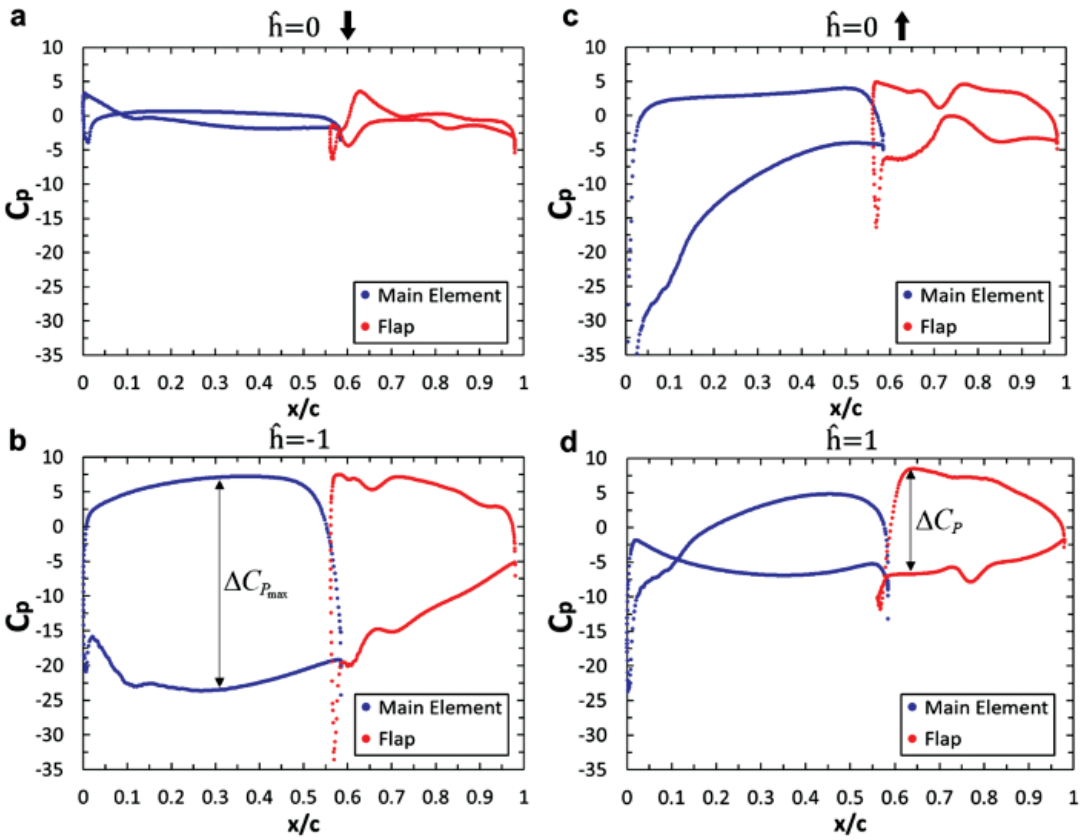

Figure 16: Surface pressure coefficient at $k = 7.48$ and $h_0/c = 0.158$ within a cycle of oscillation

At the mid-upstroke (Fig. 16c) the suction spike at the leading edge of the main element indicated the huge magnitude of the flow acceleration at this point. The ΔC_P at $\hat{h} = 0 \uparrow$ was substantially greater during the upstroke than the downstroke, due to the proximity of the suction surface to the ground and the higher curvature of the leading edge. Only one LEV was present on the pressure surface of the flap and was linked to the suction peak at $x/c = 0.71$, while the acceleration of the flow in the gap between the two elements resulted in the suction spike at the leading edge of the flap. The wider pressure peak at $x/c = 0.74$ was provoked by the shear vorticity that was compressed by the $\text{TEV}_{\text{m}}^{-}$ towards the suction surface of the flap as the wing moved upwards. At the onset of downstroke (Fig. 16d) the reverse in direction caused the reversal of the pressure distribution on the pressure and suction surfaces. The maximum increase in pressure was found at $x/c = 0.635$ on the suction surface of the flap, while the suction peak at $x/c = 0.763$ was associated with the LEV above the flap. It is of great interest that at $\hat{h} = 1$ the highest ΔC_P was found on the flap instead of the main element, and it is believed that both the onset of downstroke and the considerable amount of positive vorticity compressed under the flap, resulted in this remarkable increase in pressure.

4.7 Effect of Varying Amplitude on Wake

The second part of the present study focused on the investigation of the implications of varying amplitude in the aerodynamic behaviour of the heaving wing. Fig. 17 illustrates the wing at $h_0/c = 0.158$

and $\tau = 1$ during the downstroke at medium ($k = 1.83$) and high ($k = 7.48$) frequency, for a range of small ($a/c = 0.04$), medium ($a/c = 0.08$) and high ($a/c = 0.12$) amplitudes. At medium frequency (Fig. 17a) the wake followed a sinusoidal trend with thicker shear layers near the wing and individual separated shed vortices downstream. At large amplitude (Fig. 17a1) the vertical spread of the wake increased and the magnitude of the shed vortices was significantly enhanced by the higher vertical velocity of the wing, inducing the shear vorticity on the ground and the upward deflection of the wake. At medium amplitude (Fig. 17a2) the shed vortices became weaker and the shear layers were extended in the streamwise direction, reducing the wake thickness, whereas the wake axis was deflected slightly downwards. At the smallest amplitude (Fig. 17a3), the wake thickness decreased further and the wake axis was almost identical to the streamwise direction. The shed vortices were noticeably weaker, and the interaction with the moving ground became less intense. Moreover, the shear layer on the suction surface of the main element was expanded in the streamwise direction allowing the shear layer on the pressure surface to be extended and delay the break of the shed vortices into the wake.

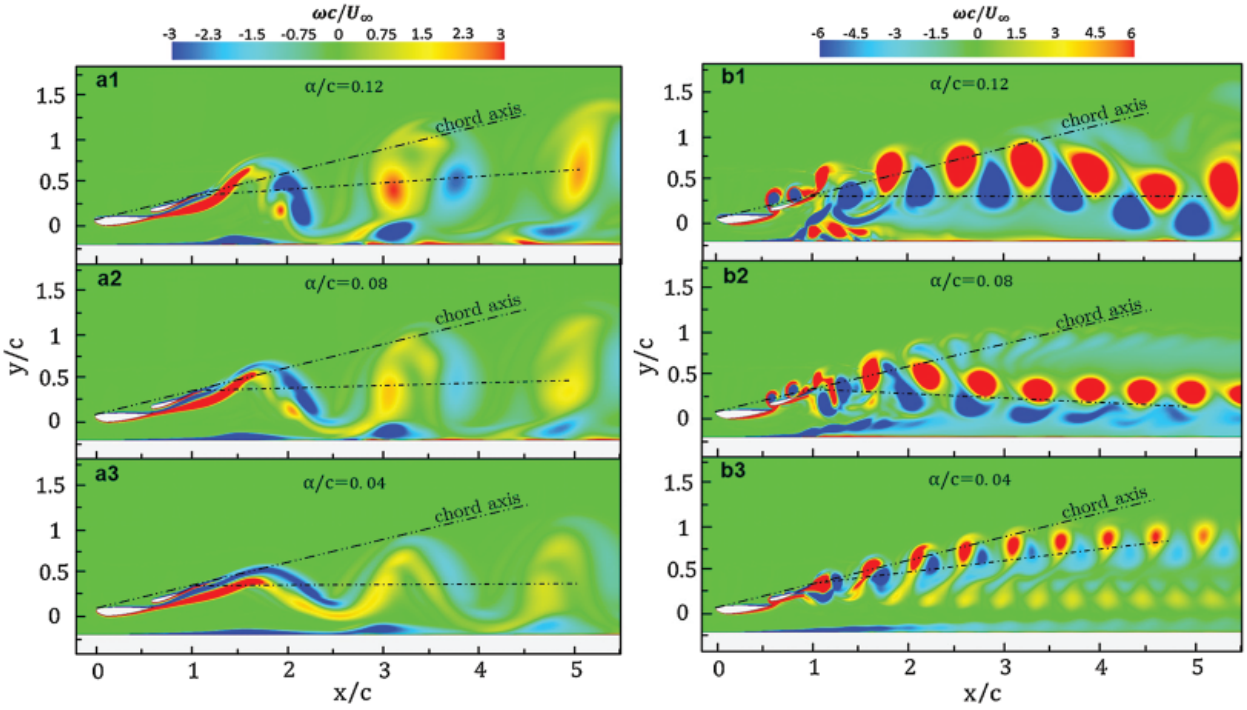

Figure 17: Contours of instantaneous non-dimensional vorticity at (a) $k = 1.83$ and (b) $k = 7.48$ at $\tau = 1$, $\hat{h} = 0$ and $h_0/c = 0.158$ for three different amplitudes

As the frequency increased (Fig. 17b), the wake consisted of cohering shed vortices with anti-clockwise rotation at the upper and clockwise rotation at the lower levels. At large amplitudes (Fig. 17b1) the higher vertical velocity enhanced substantially the magnitude of the LEV and TEV_f^+ on the flap, inducing the generation of downforce and thrust. The greater momentum of the wing lifted the shear vorticity off the ground at $x/c = 1.25$ and provoked a complex vortex shedding interaction. At medium amplitudes (Fig. 17b2), the lower vertical velocity of the wing reduced the magnitude of the shed vortices, and the direction of the wake was considerably deflected downwards as it was entrained by the moving ground. Most importantly, it was observed that for amplitudes smaller than $a/c \leq 0.05$ (Fig. 17b3) there was no evidence of the characteristic LEV and TEV_f^+ on the flap, as the shorter vertical movement of the wing

did not provide sufficient time for the positive vorticity on the suction surface of the main element to roll-up and form the LEV. The absence of the LEV and TEV_f^+ had a substantial impact on the arrangement of the shed vortices in the wake, resulting in a remarkable upshift of the wake axis towards the chord axis of the wing, as well as in a significant reduction in the magnitude of the shed vortices.

5 Conclusions

Overall an adequate qualitative and quantitative agreement between the literature and the present numerical approach was found for a range of low and high frequencies both in freestream and in ground proximity, demonstrating the accuracy of the present methodology for unsteady heaving wing simulations. The hysteresis analysis of C_L demonstrated that in proximity to the ground, the heaving motion of the double-element wing can become unstable at low frequencies, $k \leq 0.73$ since the direction of the hysteresis curves is reversed. Importantly, the hysteresis analysis of C_D provided evidence for the link between the rapid generation of thrust and the occurrence of a characteristic LEV on the flap at the onset of downstroke for frequencies, $k \geq 5.94$. The average $\bar{C}_L$ of the heaving double-element wing within a complete cycle of oscillation can be up to two times greater compared to that of a stationary wing and three times of that of a single heaving airfoil, as frequency increases and ground clearance decreases. Both for ride heights $h_0/c \geq 0.08$ and in freestream the $\bar{C}_L$ peaks at $k = 5.94$ and reduces as frequency increases further. The average $\bar{C}_D$ is consistent with that of the single airfoil, as it constantly reduces, until a critical reduced frequency k_c where drag becomes zero and thrust is produced. The value of k_c increases both with frequency and reduced ground clearance, and is the determinant factor for the ideal selection of the mean ride height and heaving frequency that would result in the optimum aerodynamic performance of the wing.

The addition of the flap results in a streamwise extension of the low-pressure region under the main element, which aids to maintain the generation of downforce for longer compared to a single heaving airfoil. However, the fundamental difference of the double-element heaving wing is found at frequencies, $k \geq 5.94$ where instead of the formation of a positive TEV on the main element during the downstroke, the occurrence of a cohering LEV and TEV_f^+ on the flap is obtained. The low-pressure cores of the LEVs on the pressure surface of the flap can locally reduce the pressure difference with the suction surface, inducing instantaneous lift during the downstroke. The magnitude of these vortices is enhanced both by increasing the frequency or amplitude of the heaving motion. On this basis, the absence of the LEV and TEV_f^+ on the flap for $k < 5.94$ leads to a characteristic sinusoidal pattern with four shear layers in the wake, whereas for amplitudes, $a/c \leq 0.05$ an arrangement of substantially weaker shed vortices and a considerable upward deflection of the wake is observed. Analysis of the instantaneous flow field in freestream revealed that at high frequencies, $k \geq 5.94$ the angle of the jet-like wake axis is near to the total angle of attack of the wing, concluding that the addition of more elements can deflect the unsteady wake further upwards under a heaving motion. On the contrary, in ground proximity, the wake deflection is found in a noticeably lower angle than the total incidence of the wing, however, by reducing the heaving amplitude $(0.12 \geq a/c \geq 0.05)$ the deflection becomes more evident especially at high frequencies, $k \geq 5.94$.

Overall, this study elucidates the broad implications of varying frequency and amplitude in the actual forces and wake structure of a double-element wing under heaving motion, which establishes a link with the aerodynamic correlation between CFD, wind tunnel and track testing in race car applications. The accuracy is limited to a 2D URANS approach, hence future research should also consider the use of advanced turbulence models such as LES or DES to obtain a more realistic representation of the unsteady flow field around the heaving wing.

Acknowledgement: The authors acknowledge the use of the IRIDIS High Performance Computing Facility, and the associated support services at the University of Southampton, in the completion of this study.

Funding Statement: The authors received no specific funding for this study.

Conflicts of Interest: The authors declare that they have no conflicts of interest to report regarding the present study.

References

1. Ansari, M. I., Anwer, S. F. (2018). Numerical analysis of an insect wing in gliding flight: Effect of corrugation on suction side. *Fluid Dynamics & Materials Processing, 14(4),* 259–279. DOI 10.32604/fdmp.2018.03891.
2. Moryossef, Y., Levy, Y. (2004). Effect of oscillations on airfoils in close proximity to the ground. *AIAA Journal, 42 (9),* 1755–1764. DOI 10.2514/1.6380.
3. Molina, J., Zhang, X. (2011). Aerodynamics of a heaving airfoil in ground effect. *AIAA Journal, 49(6),* 1168–1179. DOI 10.2514/1.J050369.
4. Badoe, C., Xie, Z. T., Sandham, N. (2019). Large Eddy simulation of a heaving wing on the Cusp of transition to turbulence. *Computers & Fluids, 184,* 64–77. DOI 10.1016/j.compfluid.2019.03.023.
5. Molina, J., Zhang, X., Angland, D. (2011). On the unsteady motion and stability of a heaving airfoil in ground effect. *Acta Mechanica Sinica, 27(2),* 164–178. DOI 10.1007/s10409-011-0445-9.
6. Theodorsen, T. (1935). General theory of aerodynamic instability and the mechanism of flutter. *NACA Technical Report, 496,* 413–433.
7. Marchesin, F. P., Barbosa, R. S., Gadola, M., Chindamo, D. (2017). High downforce race car vertical dynamics: Aerodynamic index. *Vehicle System Dynamics, 56(8),* 1269–1288. DOI 10.1080/00423114.2017.1413196.
8. Koochesfahani, M. (1989). Vortical patterns in the wake of an oscillating airfoil. *AIAA Journal, 27(9),* 1200–1205. DOI 10.2514/3.10246.
9. Jones, K., Dohring, C., Platzer, M. (1996). Wake structures behind plunging airfoils—A comparison of numerical and experimental results. *34th Aerospace Sciences Meeting and Exhibit,* 78.
10. Wang, X., Xie, Z. T. (2019). Large eddy simulation of a heaving wing in freestream turbulent flow. *11th International Symposium on Turbulence and Shear Flow Phenomena (TSFP11)*.
11. Zerihan, J. (2001). *An investigation into the aerodynamics of wings in ground effect (Ph.D. Thesis)*. UK: University of Southampton.
12. Zhang, X., Zerihan, J. (2003). Aerodynamics of a double-element wing in ground effect. *AIAA Journal, 41(6),* 1007–1016. DOI 10.2514/2.2057.
13. Siemens PLM Software (2018). STAR-CCM+ User's Manual. http://www.cd-adapco.com/products/star-ccm/documentation.
14. Wu, W., Zhou, C. (2020). A numerical study of the tip wake of a wind turbine impeller using extended proper orthogonal decomposition. *Fluid Dynamics & Materials Processing, 16(5),* 883–901. DOI 10.32604/fdmp.2020.010407.
15. Ekaterinaris, J. A., Menter, F. R. (1994). Computation of oscillating airfoil flows with one-and two-equation turbulence models. *AIAA Journal, 32(12),* 2359–2365. DOI 10.2514/3.12300.
16. Wang, S., Ingham, D. B., Ma, L., Pourkashanian, M., Tao, Z. (2010). Numerical investigations on dynamic stall of low Reynolds number flow around oscillating airfoils. *Computers & Fluids, 39(9),* 1529–1541. DOI 10.1016/j.compfluid.2010.05.004.
17. Caretto, L. S., Gosman, A. D., Patankar, S. V., Spalding, D. B. (1973). Two calculation procedures for steady, three-dimensional flows with recirculation. *Proceedings of the Third International Conference on Numerical Methods in Fluid Mechanics*. pp. 60–68. Berlin, Heidelberg: Springer.
18. Molina, J., Zhang, X., Alomar, A. (2016). Aerodynamics of a pitching and heaving airfoil in ground effect. *AIAA Journal, 54(4),* 1158–1171. DOI 10.2514/1.J053350.
19. Liang, H., Wang, X., Zou, L., Zong, Z. (2014). Numerical study of two-dimensional heaving airfoils in ground effect. *Journal of Fluids and Structures, 48,* 188–202. DOI 10.1016/j.jfluidstructs.2014.02.009.